Batteries & Supercaps

Research Article
doi.org/10.1002/batt.202300123

Chemistry Europe
European Chemical Societies Publishing

www.batteries-supercaps.org

Boosting the Electrochemical Performance of Lithium-Rich Cathodes by Oxygen Vacancy Engineering

Majid Farahmandjou,[a] Wei-Hong Lai,[b] Javad Safaei,[a] Shijian Wang,[a] Zefu Huang,[a] Frederick Marlton,[a] Jiufeng Ruan,[b] Bing Sun,[a] Hong Gao,*[a] Kostya (Ken) Ostrikov,[c] Peter H. L. Notten,[d] and Guoxiu Wang*[a]

The challenges of voltage decay and irreversible oxygen release for lithium-rich layered oxide cathode materials have hindered their commercial application despite their high energy density and low cost. Herein, a facile post-annealing strategy is developed to pre-introduce oxygen vacancies (OVs) into $Li_{1.2}Mn_{0.457}Ni_{0.229}Co_{0.114}O_2$ cathode materials. The induced OVs modify the local Mn coordination environments, enhance structural stability, and suppress oxygen release. The modified cathode exhibits a discharge capacity of 224.1 mAh g^{-1} at 0.1 C after 100 cycles with 97.7% capacity retention. Even at 2 C, excellent capacity retention of 93.3% after 300 cycles can be achieved. In situ and ex situ X-ray diffraction are used to elucidate the reaction mechanisms and crystal structure during cycling tests. Ex situ X-ray photoelectron spectroscopy confirmed the suppressed oxygen release, enhanced oxygen vacancies and reduced cathode-electrolyte interfacial layer after cycling for the post-annealed cathode. Our results show that the presence of oxygen vacancies through thermal expansion diminishes the phase transitions in cathode materials during the heating process. These findings contribute to developing next-generation Li-ion batteries (LIBs) by oxygen vacancy engineering for new cathode materials with improved electrochemical performances.

Introduction

Mn-based Li-rich layered materials $xLi_2MnO_3 \cdot (1-x)$ $LiMO_2$, M=Mn, Co, Ni, LR–MNC) are very promising cathode candidates for next-generation lithium-ion batteries due to their low cost and high energy density, which could be ascribed to the charge compensation of lattice oxygen (oxygen-related anionic redox reaction).[1–3] However, the redox reaction of lattice oxygen (with an initial charge exceeding 4.5 V) causes irreversible O_2 release and surface essential OVs leading to significant crystal structural changes and irreversible capacity loss.[4,5] In addition, the side reaction-induced electrolyte decomposition at the electrode interface would lead to voltage decay.[1,6] Numerous efforts, including surface modification,[7,8] adjustment of salt concentrations,[9,10] doping and surface coating,[11–13] have been applied to inhibit the irreversible phase transition, diminish the contact between the electrode and electrolyte, and suppress the migration of transition metals into the lithium slab.[14,15]

Ma and co-workers embedded Na ions in $Li_{1.2}Mn_{0.56}Ni_{0.16}Co_{0.08}O_2$ materials and created the surface OVs during the lithiation process.[16] Na doping can effectively accelerate lithium ion diffusivity, and the surface OVs can retard oxygen release and enhance structural stability during cycling. Accordingly, the as-prepared cathode delivers a high initial Coulombic efficiency (CE) of 84.2%. Wang et al. investigated Al/Ti co-doped $Li_{1.13}Mn_{0.517}Ni_{0.256}Co_{0.097}O_2$ by coprecipitation method.[17] The strong Al–O bonds can effectively stabilize the lattice oxygen, and the Ti^{4+} can accelerate the Li^+ transportation during cycling and decrease the bandgap of lithium layered oxides (LLOs), which can improve the capacity and rate performance. Thereby, a voltage decay of 0.34 mV per cycle and a high-capacity retention of 89.7% over 500 cycles at 1 C can be realized. Kim and coworkers demonstrated that a polydopamine (PDA) surface coating can improve the cycling performance of Li-rich Mn-rich layered cathodes.[18] PDA, a well-known oxygen radical scavenger, can provide a chemically protective layer to minimize the unwanted growth of cathode electrolyte interphase, reduce the release of oxygen gas and significantly suppress phase transformation on the surface. The formation of OVs can effectively enhance structural stability by

[a] M. Farahmandjou, J. Safaei, S. Wang, Z. Huang, Dr. F. Marlton, Dr. B. Sun, Dr. H. Gao, Prof. G. Wang
Centre for Clean Energy Technology
School of Mathematical and Physical Sciences
Faculty of Science
University of Technology Sydney
Sydney, NSW 2007 (Australia)
E-mail: hong.gao@uts.edu.au
guoxiu.wang@uts.edu.au
[b] Dr. W.-H. Lai, J. Ruan
Institute for Superconducting and Electronic Materials
University of Wollongong
Innovation Campus, Squires Way, Wollongong, NSW 2500 (Australia)
[c] Prof. K. (. Ostrikov
School of Chemistry and Physics and Centre for Materials Science
Queensland University of Technology
Brisbane, QLD 4000 (Australia)
[d] Prof. P. H. L. Notten
Eindhoven University of Technology
P.O. Box 513, 5600 MB Eindhoven (The Netherlands)

Supporting information for this article is available on the WWW under https://doi.org/10.1002/batt.202300123

Research Article
doi.org/10.1002/batt.202300123
Chemistry Europe
European Chemical Societies Publishing

suppressing O_2 release, and thus deliver excellent electrochemical performance of the lithium-rich cathodes. Oxygen vacancies can be generated in metal oxides by high-temperature annealing process under an inert or vacuum atmosphere,[19–21] which makes it possible to remove some of the metal oxide lattice oxygen at high temperatures without causing bulk phase transformation.[21,22] In this work, we introduce a facile post-annealing treatment in an argon atmosphere to introduce OVs on the surface of the $Li_{1.2}Mn_{0.457}Ni_{0.229}Co_{0.114}O_2$ cathode materials. The formation of OVs can affect the local Mn coordination environments, improve structural stability, and reduce the oxygen release from the cathode to promote its electrochemical properties. The oxygen vacancies can be tuned by varying the heat treatment temperature or inert gas flow rate during annealing process (Figure 1). A systematical investigation demonstrates that reasonable number of OVs can effectively suppress the depletion of TM ions in electrolyte and phase transition, thus realizing the structural stability, sluggish voltage decay, and improved capacity retention.

Intentional creation of oxygen vacancies in LR-MNC through a post-annealing process in argon leads to better structural stability and suppressed oxygen release which limit the voltage decay in cathodes. The suppressed oxygen release due to OVs creation diminishes the phase transitions in cathode and improve the cyclability and reversibility of Li-rich cathode during cycling. Decreasing c-lattice parameter indicates the pre-introduced OVs and shrinkage of the layer structure after post-annealing in argon.

Results and Discussion

To gain a more accurate understanding of the crystal structure, Rietveld refinement was performed. The Rietveld refinement X-ray diffraction (XRD) patterns of the LLO, and LLO-500 are shown in Figure 2(a and b). All of the samples are phase-pure without any impurity detected. The XRD patterns of the cathodes show that all peaks can be indexed to the space group R-3m with a layered hexagonal structure of α-$NaFeO_2$ except for the weak diffraction peaks between 20° and 25°, which are attributed to the superlattice monoclinic C/2 m structure of Li_2MnO_3.[23–26] The apparent splitting of the (018)/(110) peaks and (006)/(012) peaks indicate a well-ordered layered structure.[27,28] Rietveld refinement results of all samples are briefly listed in Table 1. Both LLO (1.21) and LLO-500 (1.35)

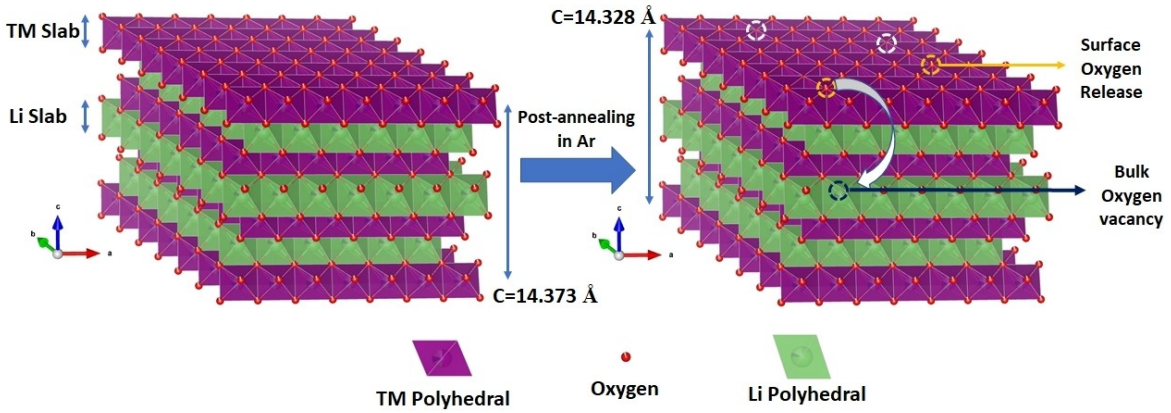

Figure 1. Schematic of surface OVs formation through post-annealing treatment.

Table 1. Comparison of Rietveld XRD refinement results of the LLO, LLO-200, LLO-300, LLO-400, LLO-500, and LLO-600 cathodes.

Sample	$LiTMO_2$ (R-3 m phase)							Li_2MnO_3 (C2/m phase)					$I_{(003)}$ / $I_{(104)}$	R_{wp} [%]
	$a=b$ [Å]	c [Å]	c/a	V [Å^3]	Composition [wt %]	Li^+/ Ni^{2+}	z [O]	a [Å]	b [Å]	c [Å]	V [Å^3]	Composition [wt %]		
LLO	2.8553 (10)	14.2450 (4)	4.9896 (66)	100.61 (8)	78.12	7.8896	0.24452	5.0052 (12)	8.590 (3)	5.049 (15)	109.2 (11)	21.18	1.21	7.03
LLO-200	2.8565 (15)	14.2501 (18)	4.9886 (05)	100.70 (17)	92.72	7.8896	0.24387	4.973 (3)	8.557 (4)	5.039 (3)	201.8 (2)	7.28	1.22	7.37
LLO-300	2.8574 (19)	14.2596 (18)	4.9950 (08)	100.83 (18)	92.98	7.8144	0.24491	5.007 (3)	8.558 (5)	5.089 (3)	206.5 (2)	7.02	1.21	6.25
LLO-400	2.8598 (18)	14.264 (2)	4.9876 (91)	101.03 (2)	93.20	7.7719	0.24667	5.048 (4)	8.526 (6)	4.975 (5)	201.7 (3)	6.80	1.25	5.75
LLO-500	2.8588 (3)	14.260 (3)	4.9881 (06)	100.94 (3)	94.47	7.7705	0.25037	4.958 (7)	8.545 (7)	5.027 (8)	201.9 (5)	5.53	1.35	6.34
LLO-600	2.8615 (2)	14.273 (3)	4.9879 (43)	101.21 (2)	87.63	7.7712	0.24695	5.050 (3)	8.575 (4)	5.051 (2)	206.8 (18)	12.37	1.23	8.10

Research Article
doi.org/10.1002/batt.202300123
Chemistry Europe
European Chemical Societies Publishing

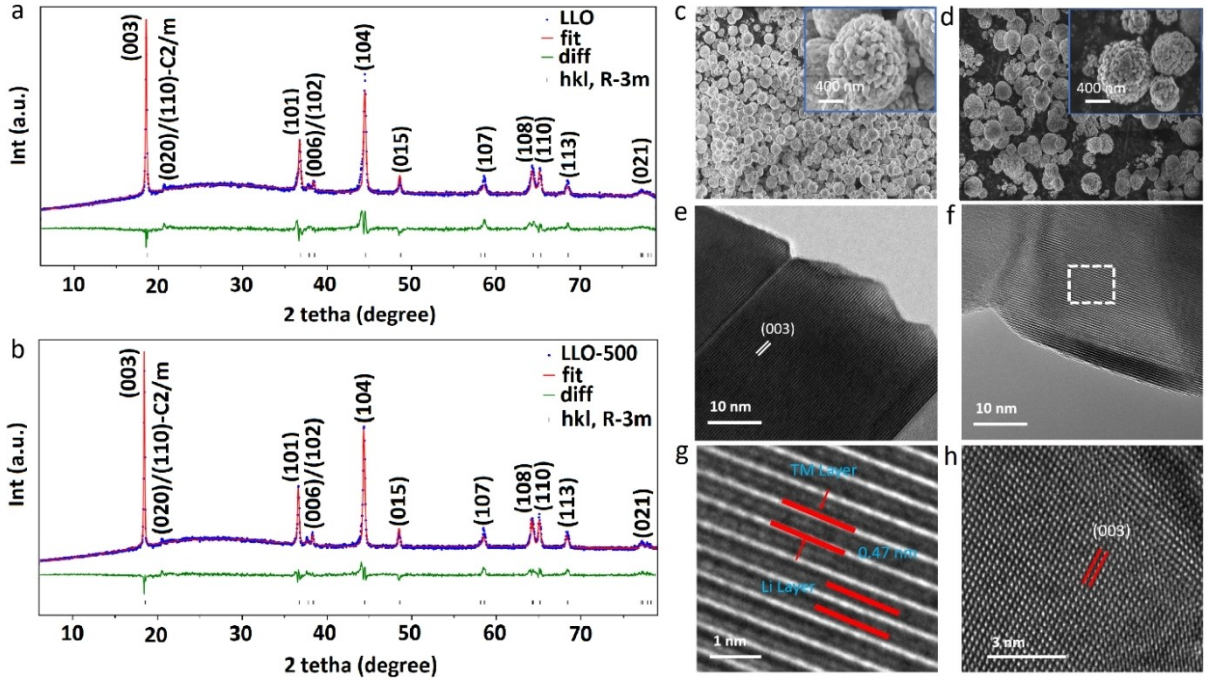

Figure 2. Refined XRD pattern of the a) LLO and b) LLO-500 cathodes; Unique morphological features associated with engineering of oxygen vacancies and layered structure, SEM images of c) LLO and d) LLO-500; TEM images of the e) LLO and f) LLO-500, corresponding g) HRTEM and h) HAADF-STEM images of LLO-500 sample.

samples have $I_{(003)}/I_{(104)}$ values over 1.2. Furthermore the *c*/*a* values of LLO (4.9896) and LLO-500 (4.9881) are larger than 4.8992, indicating the post-annealing treatment has no damage to the layer structures and Li/Ni cation mixing.[29–36] Compared to LLO (4.79114 Å), a considerable d-spacing shift in the c-axis direction can be detected in the LLO-500 sample (4.78117 Å), which can be ascribed to the pre-introduced oxygen vacancies and shrinkage of the layer structure in LLO-500 (Supporting Information, Figure S1a). Comparison of the *d*-spacing changes of the various post-annealed samples, including LLO, LLO-200, LLO-300, LLO-400, LLO-500, LLO-600, shows that the LLO-500 sample displays the largest d-spacing change due to OVs formation (see Supporting Information, Figure S1b). The Rietveld refinement of all the samples XRD patterns are presented in Supporting Information, Figure S2. All the samples could be indexed to trigonal space group R-3 m, and the weaker superstructure peaks could be indexed to monoclinic space group C2/m. Lattice parameters show no big difference between the LLO and calcined samples. This finding implies that the oxygen vacancy engineering by post annealing does not strongly influence the whole structure. After post annealing treatment, both the amount of Ni^{2+} and the occupancy of Li in the Li layer are greater than that in the pristine LLO. Interestingly, the Li^{+}/Ni^{2+} disordering decreases with an increase in Ni^{2+} content. The weighted-profile *R* value (W_{RP}) basically reflects the degree of agreement between the overall calculated intensity and the measured intensity. All W_{RP} values are less than 10, indicating excellent fit results (Table 1). In addition, both the LLO and LLO-500 samples are refined with two different local structures of R-3 m and C2/m phases. The fractions of the R-3 m and C2/m phases for LLO are 78.12% and 21.18%, while for LLO-500, the fractions of the R-3 m and C2/m phases are 94.47% and 5.53%, implying a more ordered layer structure in LLO-500 cathode. In the LLO-500 cathode, the oxygen occupancy *z*(O) refined to 0.25037 is higher than that of 0.24452 in the LLO sample, confirming less oxygen release due to OVs formation (Table 1).

Scanning electron microscopy (SEM) images of the LLO and LLO-500 are shown in Figure 2(c and d). Both LLO and LLO-500 materials display spherical morphologies, with LLO-500 having a smaller particle size (less than 1 μm). The SEM images of the samples at different post-annealing temperatures are shown in supplementary materials (Figure S3). The microstructures of the samples are further characterized by transmission electron microscopy (TEM) and high-resolution TEM (HRTEM). TEM and HRTEM images of LLO and LLO-500 are shown in Figure 3(e and f) and Figure S4, respectively. It can be concluded that both the LLO and LLO-500 samples reveal distinct lattice fringes, which is consistent with the characteristic plane (003) of α-$NaFeO_2$ (R-3m) (Figure 3e,f and Figure S4a–d). Fast Fourier transform (FFT) images of the LLO and LLO-500 samples in the supplementary materials, Figure S4(b–d) reveal that the interplanar spacing is ~0.47 nm, which is consistent with the (003) preferential peak of the layer structure. A tiny portion of rock-salt phase can be detected on the outer surface of the LLO material compared to the well-defined surface layered structure of LLO-500 (Supporting Information, Figure S4e and f). This part of the rock salt phase is responsible for the blockage of lithium-ion transport. In Figure 2(g), the distinct lattice fringes of ~0.47 nm can be observed in the HRTEM micrograph of the

Research Article
doi.org/10.1002/batt.202300123
Chemistry Europe
European Chemical Societies Publishing

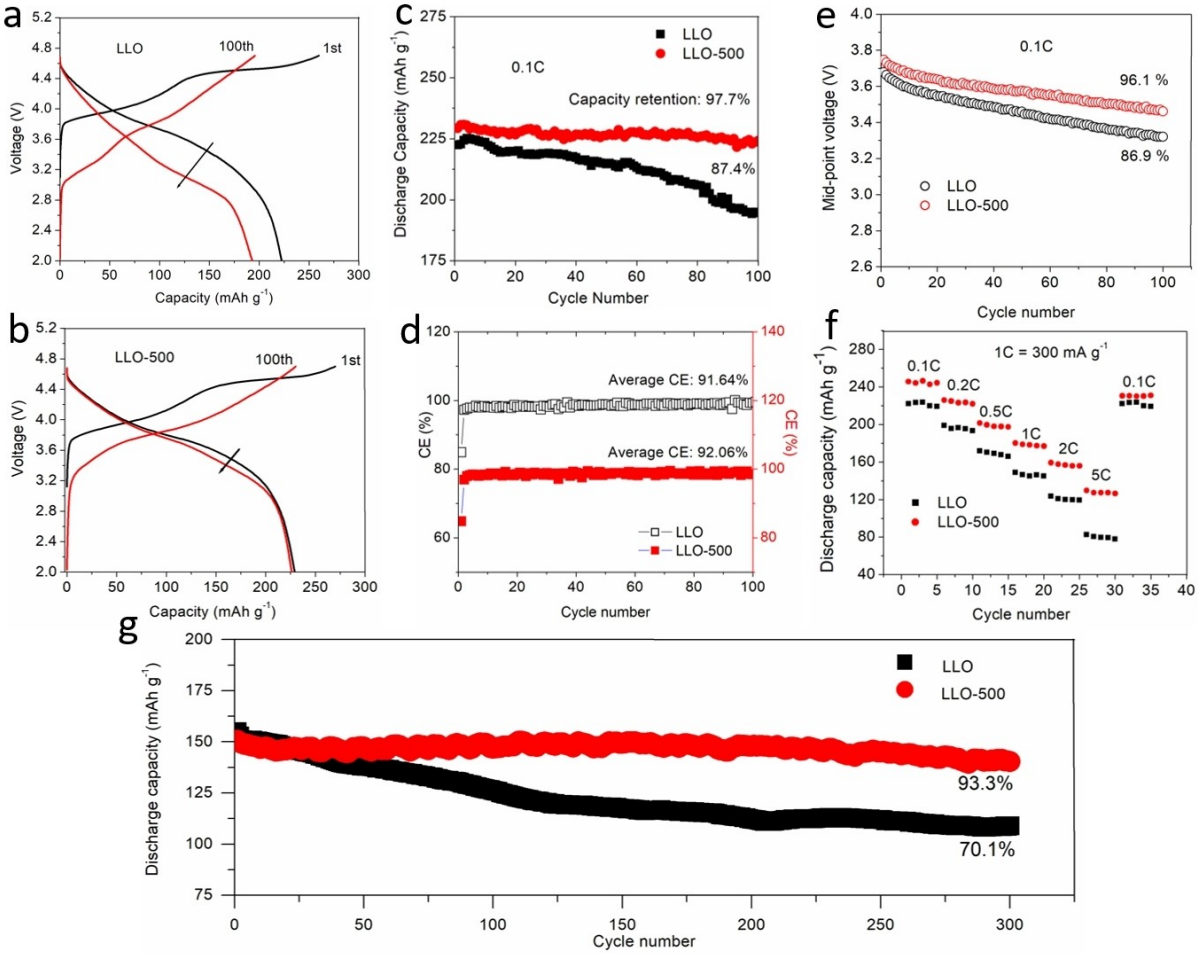

Figure 3. Electrochemical testing of the LLO cathodes. Charge/discharge profiles of a) LLO and b) LLO-500 electrodes for the first (black color) and 100th cycles (red color), half-cell cycling current density is 10 mA g^{-1} (0.1 C); c) cycling performance of LLO and LLO-500 electrodes; (d) coulombic efficiency of the LLO and LLO-500 samples at 0.1 C after 100 cycles; e) rate performance of LLO and LLO-500 at different current densities; f) mid-point voltage of the LLO and LLO-500 electrodes after 100 cycles; g) long cycling performance of the LLO and LLO-500 after 300 cycles at 2 C.

LLO-500 sample.[37–39] Furthermore, the high-angle annular dark-field (HAADF) imaging in scanning transmission electron microscopy (STEM) of the LLO-500 clearly shows that no rocksalt phase exists (Figure 2h). The STEM and the corresponding elemental mapping images of the LLO-500 sample confirm the uniform distribution of Mn, Ni, Co, and O elements (Supporting Information, Figure S5). The energy dispersive spectroscopy (EDS) analysis data of the arrow area (see Supporting Information, Figure S6) in the LLO-500 STEM is in accordance with the stoichiometry of the sample, further confirming the successful synthesis of LLO-500.

To evaluate the effect of post-annealing on the electrochemical performance of Li-rich cathode materials, systematic electrochemical tests are conducted at various current densities (1 C = 300 mA g^{-1}) in the voltage range of 2.0–4.7 V. Typical charge-discharge voltage profiles at 0.1 C for the LLO and LLO-500 electrodes are shown in Figure 3(a and b). The first charge curves for both LLO and LLO-500 consist of both a ramping voltage curve ($V \leq 4.5$ V) and a plateau voltage (4.5 V $< V \leq$ 4.7 V). The slopes result from the oxidation of Ni^{2+}/Ni^{4+} and Co^{3+}/Co^{4+},[40,41] and the plateau region above 4.5 V is ascribed to the activation of Li_2MnO_3.[40] The first charge and discharge capacities of LLO cathode are 265 and 222.4 mAh g^{-1}, respectively. The LLO-500 cathode exhibits the initial charge and discharge capacities of 275 and 229.3 mAh g^{-1}, respectively. The corresponding cycling performance of LLO shows fast capacity fading after 100 cycles with a capacity retention of 87.4%. While for the LLO-500 cathode, a very small change in the discharge capacity from 229.3 to 224.1 mAh g^{-1} can be observed under the same condition, with a capacity retention rate as high as 97.7% (Figure 3c). The small increase in initial discharge capacity may be due to the more ordered layer structure and TM oxidation in LLO-500 cathode. A higher average CE of 92.06% could be even achieved for LLO-500 compared to the LLO electrode (91.64%), which corresponds to a high utilization of the total lithium content (Figure 3d). The cycling performance of the samples annealed at different temperatures was carried out as well (Supporting Information, Figure S7a). The rate capabilities of LLO, LLO-200, LLO-300, LLO-400, LLO-500, and LLO-600 are investigated (Figure 3e and Supporting Information, Figure S7b–d). Obviously, the rate performance increases with the calcination temperature, and all

Research Article
doi.org/10.1002/batt.202300123
Chemistry Europe
European Chemical Societies Publishing

samples show good capacity retention after the current density returns to 0.1 C. LLO-500 achieves discharge capacities of 241, 223, 198, 174, 151, and 125 mAh g^{-1} at current densities of 0.1, 0.2, 0.5, 1, 2, and 5 C, respectively. The capacities of the LLO samples under the same conditions are 228, 210, 187, 162, 137 and 75 mAh g^{-1}, respectively. Figure 3(f) exhibits the mid-point voltage of LLO and LLO-500 cathodes at 0.1 C. The voltage retention of LLO and LLO-500 is 86.9% and 96.1%, respectively, after 100 cycles. The smaller voltage fading is due to less oxygen release and better electron transport of the LLO-500 sample. At a high current density of 2 C, the capacity retention of the LLO-500 electrode was as high as 93.3% after 300 cycles while that of the LLO electrode was only 70.1% (Figure 3g), indicating a strong structural stability of the LLO-500 sample. The voltage profiles of the LLO and LLO-500 electrode (Supporting Information, Figure S8), indicates less capacity fading of the LLO-500 sample due to less Li^+/Ni^{2+} mixing and more crystal stability.

Cyclic voltammetry (CV) is performed to study the redox process of the synthesized materials within a voltage range of 2.0 to 4.7 V at 0.1 mV/s scan rate. Figure 4(a and b) displays the initial five CV curves of the LLO and LLO-500 cathodes, both of which feature the unique CV peaks of Li-rich cathode materials, namely the LLO-200, LLO-300, LLO-400, and LLO-600 cathode materials (Supporting Information, Figure S9).[16,42–45] During the initial charge, the peak located at ~4.0 V corresponds to the oxidation of Ni^{2+}/Ni^{4+} and Co^{3+}/Co^{4+}, which shows an increased intensity in the following charge, indicating activated electron transport.[46,47] While the other peak at ~4.6 V is attributed to the activation of Li_2MnO_3, which weakens in subsequent cycles, indicating that Li^+ is irreversibly removed from Li_2MnO_3 in the form of Li_2O.[16,43] The corresponding reduction peaks of Ni^{4+}/Ni^{3+} and Co^{4+}/Co^{3+} are detected at 3.73 V and 4.37 V, respectively. The peak located at 3.26 V is ascribed to the reduction of Mn^{4+}/Mn^{3+}, which becomes apparent during cycling, manifesting a gradual increase in capacity.[43–45] There are small changes for such a peak for LLO, suggesting that LLO suffers from capacity fading during cycling due to the total activation of Li_2MnO_3 during the first cycle,[16] as shown in Figure 4(a). Additionally, the average voltage fading at 3.73 V for LLO and LLO-500 from the first to the fifth cycle is 0.034 and 0.017 V, respectively, indicating a better stability for LLO-500. Interestingly, the differences values between the anodic and cathodic peaks were 0.32 V and 0.12 V for the LLO-500 cathode at the first and fifth cycles, respectively, compared to 0.34 V and 0.17 V for LLO (Figures 4c and d). This result confirms that LLO-500 has a better redox reversibility than LLO.

Electrochemical impedance spectroscopy (EIS) studies were carried out during cycling to investigate the reaction kinetics and electrochemical characteristics of the electrode materials prepared at different temperatures during cycling. High/intermediate-frequency semicircles and low-frequency tails were found in the initial and the fifth cycle (Supporting Information, Figures S10). The high-frequency semicircle exhibits the resistance of the solid electrolyte interface (SEI) layer.[48] In contrast, the intermediate-frequency semicircle is related to the charge-transfer resistance at the cathode/electrolyte interface (CEI) layer, and the low-frequency tail is ascribed to Li^+ ion diffusion.[49,50] The fitted results show that during the first cycle charged to 4.7 V, the resistance decreases from 320 to 120 Ω for the LLO and LLO-500 electrodes, respectively. After the five cycles, the two electrodes show a similar SEI layer resistance. The resistance decreases from 125 to 70 Ω for LLO and LLO-

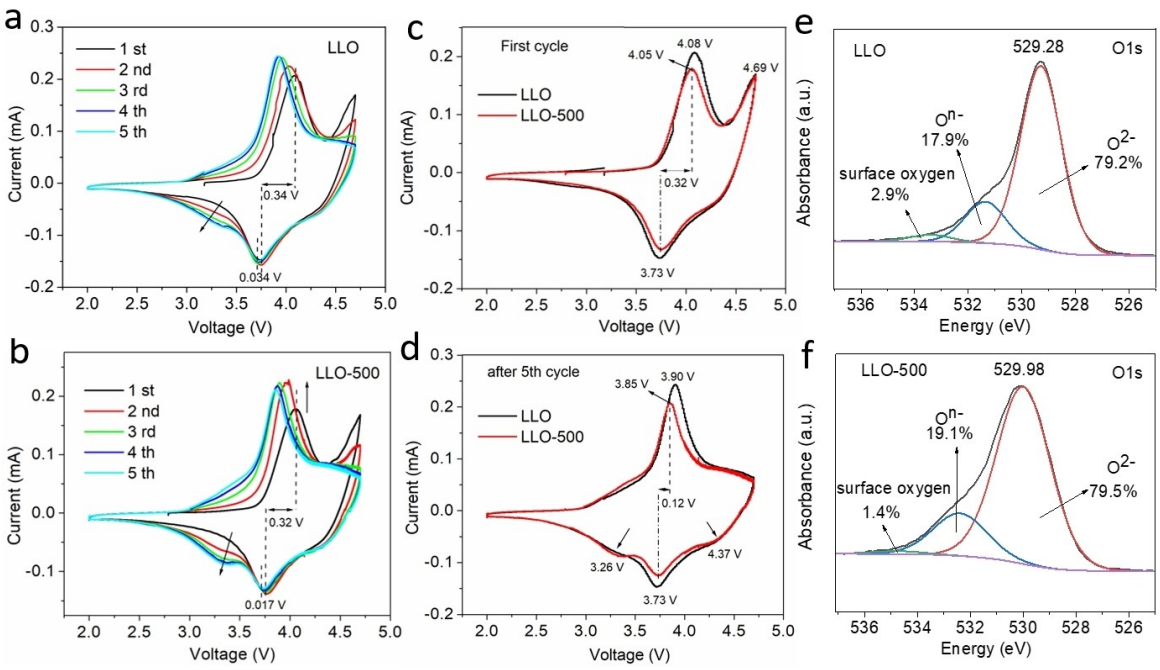

Figure 4. CV of the first 5 cycles of the a) LLO and b) LL0-500 cathodes; comparison of CV profiles of the LLO and LLO-500 cathodes c) at the first cycle, and d) after 5 cycles; electronic structure of Li-rich layered cathode materials, XPS spectra of O 1s for e) LLO and f) LLO-500 samples.

500, respectively, indicating a thinner CEI layer for the LLO-500 sample. The larger charge-transfer resistance for the LLO sample is likely to be the main reason for the capacity fading because of the enhanced kinetic barrier for lithium extraction/insertion. Collectively, these results reveal that the best electrochemical properties are obtained with the LLO-500 cathode because of the well-defined layered structure, active Li-ion kinetics, strong crystal stability, and reduced cation mixing.

To study the variation in the surface chemical states of TM and O after post-annealing, the X-ray photoelectron spectroscopy (XPS) measurements were carried out. The measured spectra of Figure S11 clearly display the existence of Li, Ni, Co, Mn, C, and O elements. Figure 4(e and f) shows the O1s XPS spectra of the LLO and LLO-500 samples. It is evident that the presence of oxygen vacancies O^{n-} ($0 < n < 1$) on the surface of LLO-500 (19.1%) is higher than that of the LLO (17.9%), and the surface oxygen content is reduced (1.4%),[16,18] suggesting that most of the residual active oxygen species (Li_2CO_3/LiOH) are reduced after the post annealing process in argon atmosphere. This is beneficial to inhibit the TM migration to the Li layer thereby improving the crystal stability. Additionally, the prominent O 1s peak at 529.28 eV, corresponding to the lattice oxygen O^{2-} of the LLO, gradually shifts to higher binding energy (529.98 eV) in the LLO-500 sample, which can be attributed to a suppressed spinel phase transformation. Compare with LLO, LLO-200, LLO-300, LLO-400, LLO-600, the LLO-500 sample presents the largest relative area of the oxygen vacancy (O^{n-}) to surface oxygen (13.64), indicating less oxygen release due to OVs formation (Supporting Information, Figure S12 and Table 2). Additionally, the STEM and the corresponding EDX line scans images of the LLO and LLO-500 samples demonstrate that the LLO-500 possess less O atoms, thus apparently indicating the reduced oxygen release from the surface of the cathode after calcination in argon (Supporting Information, Figure S13). Figure S14 (a, b) show the XPS spectra of Mn 2p for LLO and LLO-500 samples. There is not much difference in the Mn 2p spectra between LLO and LLO-500. The peak of Mn $2p_{3/2}$ and Mn $2p_{1/2}$ is located at 641.98 eV and 653.63 eV, respectively.[16,18] The content of Mn^{4+} in LLO-500 (14.6%) is less than that of LLO (14.1%), thus indicating that more redox reaction of Mn atoms and less dissolution of Mn in the Li layer. For the Ni 2p spectrum, the peak corresponding to the Ni $2p_{3/2}$ state can be deconvoluted into two peaks, located at 856.88 eV and 854.58 eV, ascribed to Ni^{3+} and Ni^{2+} states, respectively.[51,52] The small peak area of Ni^{3+} corresponding to LLO (12.7%) is larger than that of LLO-500 (10.4%), which may be due to the enhanced oxygen vacancies of LLO-500 resulting in the compensation of Ni^{2+} ions from Ni^{3+} ions, trapping the Ni ions to avoid transform to Li layer,[38,39,53] increasing the transport of Li ions to the Li layer, and then enhance the electron transport and electrochemical performance.[38,39] Figure S15 shows the oxygen vacancy dependence of the samples in different temperatures. It can be seen that the concentration of the oxygen vacancy increases as the annealing temperature rises from 200 to 500 °C and then decreases as the temperature rises to 600 °C. These results show that LLO-500 has higher oxygen activity.

The ex situ and in situ systematic studies were further carried out to elaborate the reaction mechanism and crystal evaluation during cycling. Figure 5(a and b) reveals ex situ SEM images of the LLO and LLO-500 samples after 100 cycles, respectively. LLO-500 is free of cracks and particle shape deformation, indicating that it is more stable than the LLO sample. Ex situ XRD was performed to investigate possible structural changes after cycling. Figure 5(c) displays ex situ XRD spectra of LLO and LLO-500 electrode charged to 4.7 V after 100 cycles. The intensity ratio of both $I_{(003)}/I_{(104)}$ for LLO (1.29) and LLO-500 (1.42) are still over 1.2. There is no obvious change for both LLO and LLO-500 after cycling compared to the corresponding XRD spectra of the untreated samples. The *d*-spacing of (003) plane shifts to 4.83658 Å for LLO-500 compared to that of 4.823337 Å for the LLO sample, indicating more effective transport of Li^+ ions and reduced voltage decay for LLO-500, as shown in Figure 5(d). The ex situ XRD results reveal that the LLO-500 sample still exhibits a clear splitting between the (006)/(012) and (108)/(110) diffraction peaks; these findings indicate that the sintering temperature is beneficial to the formation of layered structures.[27,28] It is reasonable to expect that after charging to 4.7 V, the electrostatic repulsion between oxygen layers would be activated, shielded by Li atoms before charging. It can also be seen that the peak corresponding to the superlattice ordering of Li_2MnO_3 disap-

Table 2. Comparison of the XPS data including O1s, Mn2p and Ni2p of the LLO, LLO-200, LLO-300, LLO-400, LLO-500, and LLO-600 cathode materials.

Sample No.	Oxygen lattice (O^{2-}) Binding energy [eV]/relative areal [%]	Oxygen vacancy (O^{n-})	Surface oxygen	Oxygen vacancy (O^{n-})/surface oxygen	Mn^{3+} (2p 3/2)	Mn^{4+} 2p 3/2	Ni^{2+} 2p 3/2	Ni^{3+} 2p 3/2
LLO	529.28/79.2	531.38/17.9	533.48/2.9	6.17	641.98/85.4	644.78/14.6	854.58/50.5	856.78/12.7
LLO-200	529.78/62.4	531.78/26.2	533.38/11.4	2.3	642.48/84.0	645.18/16	855.28/52.0	857.68 12.2
LLO-300	529.80/69.0	532.08/22.3	533.58/8.7	2.56	642.68/86.7	645.48/13.3	855.18/50.3	857.28/12.9
LLO-400	529.38/72.3	531.48/22.9	533.28/4.8	4.77	641.98/85.2	644.78/14.8	854.78/50.0	856.98/13.1
LLO-500	529.98/79.5	532.48/19.1	534.78/1.4	13.64	642.68/85.9	645.28/14.1	855.28/54.1	857.98/10.4
LLO-600	529.38/62.6	531.48/32.9	533.18/4.5	4.73	641.88/86.3	644.68/13.7	854.68/48.6	856.78/13.6

Research Article
doi.org/10.1002/batt.202300123
Chemistry Europe
European Chemical Societies Publishing

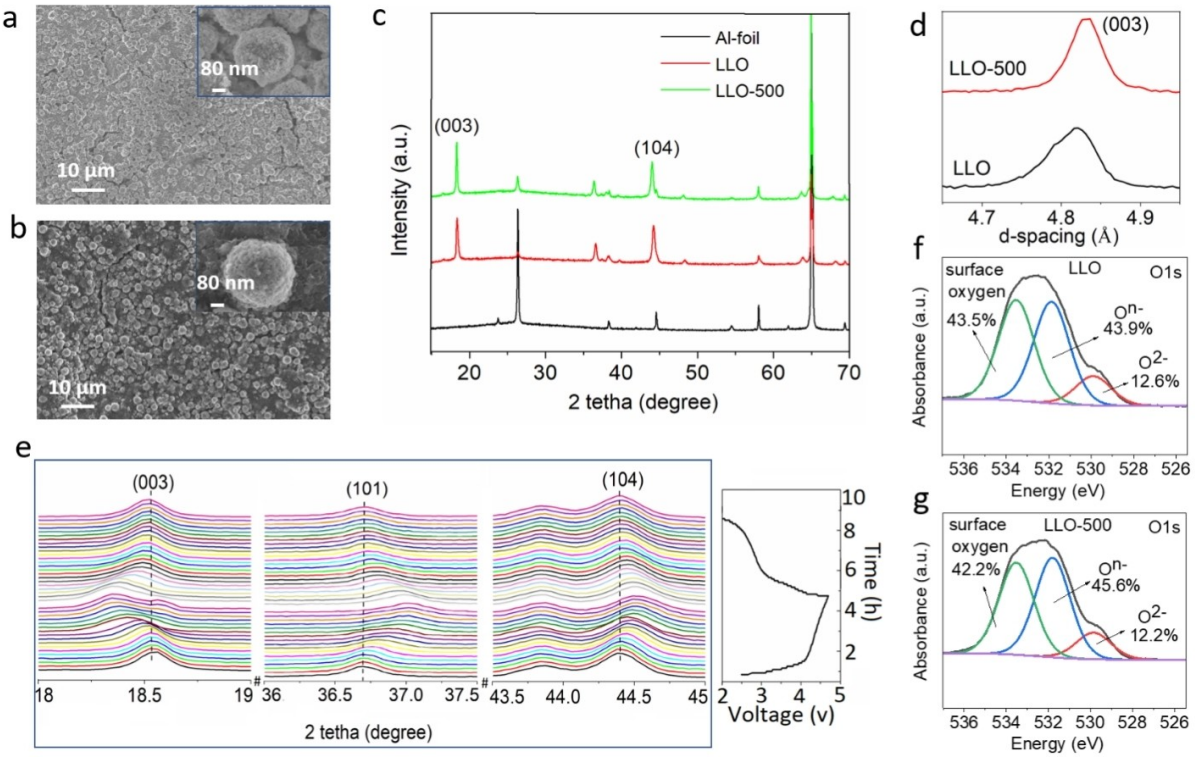

Figure 5. Ex-situ and in-situ evidence of LLO Cathodes. a) Ex situ SEM images of a) LLO and b) LLO-500 samples after 100 cycles. c) The ex situ XRD pattern of LLO and LLO-500 cathodes charged to 4.7 V after 100 cycles; d) *d*-spacing of the LLO and LLO-500 charged to 4.7 V after 100 cycles; e) in situ XRD of LLO-500 cathode for the first cycle, with corresponding initial charge-discharge curve; ex situ XPS spectra of O 1s for f) LLO and g) LLO-500 charged to 4.7 V after 100 cycles.

pears, confirming the activation process of Li_2MnO_3[23–26] as can be seen in Figure 5(c).

To further investigate the crystal structure changes during charge and discharge process, in situ XRD measurements were performed at voltages between 2 and 4.7 V during the first cycle (Figure 5e). It can be seen that the (003) peak shifts to a lower diffraction angle, while the (101) and (104) peaks shift to a higher diffraction angle during the initial charge process. This observation can be attributed to the increase of the lattice parameter c due to the increased electrostatic repulsion of the adjacent oxygen layer, and the shrinkage of the TM-TM distance due to the shortening of the TM–O bond due to Li^+ extraction.[56–58] During the discharge, the diffraction peaks shift in the opposite direction upon the insertion of Li^+. The peak shift to the original position for the LLO-500 (dashed line) is caused by the reversible oxygen atom O^{2-} and the reversible TM migration from the octahedral position of the rigid TM layer to the octahedral position of the Li^+ layer. This leads to stabilization of structure and voltage.[40] It is worth noting that the peaks are almost stable for the LLO-500 cathode, thereby indicating less oxygen release.

Furthermore, the ex situ XPS was carried out to investigate the valence state of cathode materials after 100 cycles. Figure 5(f and g) shows the ex situ O1s XPS results for the LLO and LLO-500 samples in the charged state of 4.7 V after 100 cycles. Compared to the XPS spectra of the untreated LLO and LLO-500 samples, the binding energy changes between the lattice oxygen (O^{2-}) and oxygen vacancy (O^{n-}) states can be observed in the LLO and LLO-500 samples after cycling. The intensity of the binding energies at 529.88 eV significantly decreases, which confirms that the number of oxygen vacancy increases after charging to 4.7 V. It is evident that the surface oxygen content at 533.58 eV for the LLO-500 (42.2%) is reduced compared to the LLO (43.5%), suggesting less oxygen loss even after cycling. These results indicate that less parasitic reactions occur on the surface of LLO-500 cathode than LLO cathode.

Conclusions

In this study, a facile post-annealing process in an argon atmosphere is conducted to pre-introduce oxygen vacancies (OVs) on the surface of $Li_{1.2}Mn_{0.457}Ni_{0.229}Co_{0.114}O_2$ cathode oxide materials. The post-annealing in argon was found to play important roles on the layered structure, crystallinity, and electrochemical performance of the samples. Compared to the pristine LLO, the post-annealed LLO-500 materials with pre-introduced OVs inherits less cation mixing and enlarged Li slabs. Consequently, the corresponding cathodes display a mitigated voltage decay, reduced electrochemical resistance, and excellent electrochemical performance. The as-prepared LLO-500 cathode delivers a high discharge capacity of 224.1 mAh g^{-1} at 0.1 C after 100 cycles with 97.7% capacity retention. Even at 2 C, a superior capacity retention of 93.3%

Research Article
doi.org/10.1002/batt.202300123

after 300 cycles can be achieved. Ex situ XPS study reveals that after 100 cycles, the parasitic reactions occurring in the LLO-500 cathode are greatly decreased, confirming the excellent stability and suppressed oxygen release. In situ XRD of LLO-500 demonstrates the reversible crystal structure during the charge and discharge process. This post-annealing strategy provides valuable insights for the development of high-performance and high-safety Li-rich cathode materials.

Experimental Section

The $Li_{1.2}Mn_{0.457}Ni_{0.229}Co_{0.114}O_2$ was first prepared by hydrothermal method and then by a solid-state method. Stoichiometric amounts of Ni/Mn/Co sulfate, polyvinylpyrrolidone (PVP, surfactant), and sodium bicarbonate (precipitant) aqueous solution were mixed in appropriate ratios to obtain the carbonate precursor $Mn_{4/6}$ $Ni_{2/7}Co_{1/7}CO_3$. Firstly, 4.0 mmol $MnSO_4 \cdot 4H_2O$, 2.0 mmol $NiSO_4 \cdot 4H_2O$, 1.0 mmol $CoSO_4 \cdot 4H_2O$, 0.4 g polyvinylpyrrolidone (PVP) and 4.0 mmol ascorbic acid were dissolved into a mixed solvent of 60.0 mL of water and 60.0 mL of triethylene glycol (TEG). The above solution was then transferred into a polytetrafluoroethylene (PTFE) container, sealed in and placed in a stainless-steel autoclave and held at 180 °C for 12 h. After cooling to room temperature, a purple precipitate was obtained, which was then washed with deionized water and centrifuged. the precipitate was then dried at 80 °C overnight. After that, the carbonate precursor was mixed with Li_2CO_3 in a stochiometric ratio and heated to 800 °C in air for 12 h at a heating rate of 5 °C min^{-1}. In the second step, the black product (LLO sample) was then sintered under argon at different temperatures of 200, 300, 400, 500 and 600 °C at a heating rate of 5 °C/min for 30 min to achieve the final Li- and Mn-rich cathode materials (named as LLO-200, LLO-300, LLO-400, LLO-500 and LLO-600). Afterward, the synthesized powder was naturally cooled down to room temperature (25 °C). Finally ground in a mortar for further characterization. The cell assembling and characterization details are provided in the Supporting Information.

Supporting Information

Supporting Information is available from the Wiley Online Library or from the author.

Acknowledgements

We would like to acknowledge financial support from the Australian Research Council (ARC) Discovery Project (DP200101249) and ARC Research Hub for Integrated Energy Storage Solutions (IH180100020). K.O. acknowledges partial support from the Australian Research Council (ARC) and QUT Centre for Materials Science. Open Access publishing facilitated by University of Technology Sydney, as part of the Wiley - University of Technology Sydney agreement via the Council of Australian University Librarians.

Conflict of Interest

The authors declare no conflict of interest.

Data Availability Statement

The data that support the findings of this study are available from the corresponding author upon reasonable request.

Keywords: lithium-rich cathode · oxygen release · oxygen vacancy · post-annealing treatment · redox process

[1] D. Eum, B. Kim, S. J. Kim, H. Park, J. Wu, S.-P. Cho, G. Yoon, M. H. Lee, S.-K. Jung, W. Yang, *Nat. Mater.* **2020**, *19*, 419.
[2] S. Zhao, Z. Guo, J. Yang, C. Wang, B. Sun, G. Wang, *Small* **2021**, *17*, 2007431.
[3] Y. Liu, Y. Zhu, Y. Cui, *Nat. Energy* **2019**, *4*, 540.
[4] J. Lan, Q. Zheng, H. Zhou, J. Li, L. Xing, K. Xu, W. Fan, L. Yu, W. Li, *ACS Appl. Mater. Interfaces* **2019**, *11*, 28841.
[5] S. Lou, Y. Ma, Z. Zhou, H. Huo, P. Zuo, X. Cheng, X. Qu, Y. Gao, C. Du, G. Yin, *ChemElectroChem* **2018**, *5*, 1569.
[6] H. Guo, Z. Wei, K. Jia, B. Qiu, C. Yin, F. Meng, Q. Zhang, L. Gu, S. Han, Y. Liu, *Energy Storage Mater.* **2019**, *16*, 220.
[7] C. Yin, X. Wen, L. Wan, Z. Shi, Z. Wei, X. Li, Q. Gu, B. Qiu, Z. Liu, *J. Power Sources* **2021**, *503*, 230048.
[8] B. Xiao, X. Sun, *Adv. Energy Mater.* **2018**, *8*, 1802057.
[9] B. Ravikumar, M. Mynam, B. Rai, *J. Phys. Chem. C* **2018**, *122*, 8173.
[10] J. Lee, D. Yu, Z. Zhu, X. Yao, C. Wang, Y. Dong, R. Malik, J. Li, *ACS Appl. Energ. Mater.* **2020**, *3*, 7931.
[11] P. Vanaphuti, Y. Liu, X. Ma, J. Fu, Y. Lin, J. Wen, Z. Yang, Y. Wang, *ACS Appl. Mater. Interfaces* **2021**, *13*, 22597.
[12] X. D. Zhang, J. L. Shi, J. Y. Liang, Y. X. Yin, J. N. Zhang, X. Q. Yu, Y. G. Guo, *Adv. Mater.* **2018**, *30*, 1801751.
[13] Q. Fan, K. Lin, S. Yang, S. Guan, J. Chen, S. Feng, J. Liu, L. Liu, J. Li, Z. Shi, *J. Power Sources* **2020**, *477*, 228745.
[14] B. Xiao, B. Wang, J. Liu, K. Kaliyappan, Q. Sun, Y. Liu, G. Dadheech, M. P. Balogh, L. Yang, T.-K. Sham, *Nano Energy* **2017**, *34*, 120.
[15] K. McColl, R. A. House, G. J. Rees, A. G. Squires, S. W. Coles, P. G. Bruce, B. J. Morgan, M. S. Islam, *Nat. Commun.* **2022**, *13*, 1.
[16] Q. Ma, Z. Chen, S. Zhong, J. Meng, F. Lai, Z. Li, C. Cheng, L. Zhang, T. Liu, *Nano Energy* **2021**, *81*, 105622.
[17] E. Wang, D. Xiao, T. Wu, X. Liu, Y. Zhou, B. Wang, T. Lin, X. Zhang, H. Yu, *Adv. Funct. Mater.* **2022**, *32*, 2201744.
[18] S. Y. Kim, C. S. Park, S. Hosseini, J. Lampert, Y. J. Kim, L. F. Nazar, *Adv. Energy Mater.* **2021**, *11*, 2100552.
[19] K. Zhu, F. Shi, X. Zhu, W. Yang, *Nano Energy* **2020**, *73*, 104761.
[20] M. Al-Hashem, S. Akbar, P. Morris, *Sens. Actuators B* **2019**, *301*, 126845.
[21] Z.-K. Tang, Y.-F. Xue, G. Teobaldi, L.-M. Liu, *Nanoscale Horiz.* **2020**, *5*, 1453.
[22] A. Ruiz Puigdollers, P. Schlexer, S. Tosoni, G. Pacchioni, *ACS Catal.* **2017**, *7*, 6493.
[23] Z. Lu, D. MacNeil, J. Dahn, *Electrochem. Solid-State Lett.* **2001**, *4*, A200.
[24] M. M. Thackeray, S.-H. Kang, C. S. Johnson, J. T. Vaughey, R. Benedek, S. Hackney, *J. Mater. Chem.* **2007**, *17*, 3112.
[25] W. Lee, S. Muhammad, C. Sergey, H. Lee, J. Yoon, Y. M. Kang, W. S. Yoon, *Angew. Chem. Int. Ed.* **2020**, *59*, 2578.
[26] A. Manthiram, J. C. Knight, S. T. Myung, S. M. Oh, Y. K. Sun, *Adv. Energy Mater.* **2016**, *6*, 1501010.
[27] F. Zhang, S. Lou, S. Li, Z. Yu, Q. Liu, A. Dai, C. Cao, M. F. Toney, M. Ge, X. Xiao, *Nat. Commun.* **2020**, *11*, 1.
[28] J. Xia, M. Huang, Z. Peng, G. Hu, K. Du, J. Zeng, H. Su, Y. Cao, *Solid State Ionics* **2021**, *371*, 115757.
[29] F. Wu, Q. Xue, L. Li, X. Zhang, Y. Huang, E. Fan, R. Chen, *RSC Adv.* **2017**, *7*, 1191.
[30] C. Shen, Y. Liu, L. Hu, W. Li, X. Liu, Y. Shi, Y. Jiang, B. Zhao, J. Zhang, *Nano Energy* **2022**, *101*, 107555.
[31] W. Liu, P. Oh, X. Liu, M. J. Lee, W. Cho, S. Chae, Y. Kim, J. Cho, *Angew. Chem. Int. Ed.* **2015**, *54*, 4440.

[32] T. Ohzuku, A. Ueda, M. Nagayama, Y. Iwakoshi, H. Komori, *Electrochim. Acta* **1993**, *38*, 1159.
[33] N. Li, M. Sun, W. H. Kan, Z. Zhuo, S. Hwang, S. E. Renfrew, M. Avdeev, A. Huq, B. D. McCloskey, D. Su, *Nat. Commun.* **2021**, *12*, 1.
[34] E. Antolini, *Solid State Ionics* **2004**, *170*, 159.
[35] J. Li, G. Liang, W. Zheng, S. Zhang, K. Davey, W. K. Pang, Z. Guo, *Nano. Mater. Sci.* **2022**, DOI: 10.1016/j.nanoms.2022.09.001.
[36] P. Xiao, W. Li, S. Chen, G. Li, Z. Dai, M. Feng, X. Chen, W. Yang, *ACS Appl. Mater. Interfaces* **2022**, *14*, 31851.
[37] W. He, P. Liu, B. Qu, Z. Zheng, H. Zheng, P. Deng, P. Li, S. Li, H. Huang, L. Wang, *Adv. Sci.* **2019**, *6*, 1802114.
[38] F. Guo, Y. Xie, Y. Zhang, *Nano Res.* **2022**, *15*, 8962.
[39] P. Reale, D. Privitera, S. Panero, B. Scrosati, *Solid State Ionics* **2007**, *178*, 1390.
[40] H. Liu, Y. Chen, S. Hy, K. An, S. Venkatachalam, D. Qian, M. Zhang, Y. S. Meng, *Adv. Energy Mater.* **2016**, *6*, 1502143.
[41] J. Zhang, Q. Zhang, D. Wong, N. Zhang, G. Ren, L. Gu, C. Schulz, L. He, Y. Yu, X. Liu, *Nat. Commun.* **2021**, *12*, 1.
[42] F. Ding, J. Li, F. Deng, G. Xu, Y. Liu, K. Yang, F. Kang, *ACS Appl. Mater. Interfaces* **2017**, *9*, 27936.
[43] F. Meng, H. Guo, Z. Wang, X. Li, Y. Deng, *Ionics* **2020**, *26*, 2117.
[44] F. Li, Y. Wang, S. Gao, P. Hou, L. Zhang, *J. Mater. Chem. A* **2017**, *5*, 24758.
[45] Y. Chen, X. Wang, J. Zhang, B. Chen, J. Xu, S. Zhang, L. Zhang, *RSC Adv.* **2019**, *9*, 2172.
[46] B. Liu, Z. Zhang, J. Wan, S. Liu, *Ionics* **2017**, *23*, 1365.
[47] K. I. Hamad, Y. Xing, *Batteries* **2019**, *5*, 69.
[48] H. Lee, C. Wan, Y. Wang, *J. Electrochem. Soc.* **2004**, *151*, A542.
[49] R. Pathak, K. Chen, A. Gurung, K. M. Reza, B. Bahrami, J. Pokharel, A. Baniya, W. He, F. Wu, Y. Zhou, *Nat. Commun.* **2020**, *11*, 1.
[50] S. Liu, X. Ji, N. Piao, J. Chen, N. Eidson, J. Xu, P. Wang, L. Chen, J. Zhang, T. Deng, *Angew. Chem. Int. Ed.* **2021**, *60*, 3661.
[51] H. Zhao, W. Li, J. Li, H. Xu, C. Zhang, J. Li, C. Han, Z. Li, M. Chu, X. Qiu, *Nano Energy* **2022**, *92*, 106760.
[52] Y. Liang, S. Li, J. Xie, L. Yang, W. Li, C. Li, L. Ai, X. Fu, X. Cui, X. Shangguan, *New J. Chem.* **2019**, *43*, 12004.
[53] X. Xu, L. Li, J. Huang, H. Jin, X. Fang, W. Liu, N. Zhang, H. Wang, X. Wang, *ACS Catal.* **2018**, *8*, 8033.
[54] B. Qiu, M. Zhang, L. Wu, J. Wang, Y. Xia, D. Qian, H. Liu, S. Hy, Y. Chen, K. An, Y. Zhu, *Nat. Commun.* **2016**, *7*, 12108.
[55] S. Chong, Y. Liu, W. Yan, Y. Chen, *RSC Adv.* **2016**, *6*, 53662.
[56] Q. Li, D. Ning, D. Zhou, K. An, G. t Schuck, D. Wong, W. Kong, C. Schulz, G. Schumacher, X. Liu, *Chem. Mater.* **2020**, *32*, 9404.
[57] M. Farahmandjou, S. Zhao, W. H. Lai, B. Sun, P. H. L. Notten, G. Wang, *Nano Mater. Sci.* **2022**, *4*, 322.
[58] T. Lin, T. U. Schulli, Y. Hu, X. Zhu, Q. Gu, B. Luo, B. Cowie, L. Wang, *Adv. Funct. Mater.* **2020**, *30*, 1909192.

Manuscript received: March 24, 2023
Accepted manuscript online: April 3, 2023
Version of record online: April 19, 2023